Correspondence to:
W. Wei,
weiww@cma.gov.cn

Energy Spectra Variations of Energetic Ions Associated With a Stream Interaction Region

Wenwen Wei[1,2,3] , Bin Zhuang[4], Jia Huang[5] , Fang Shen[6] , Lulu Zhao[5], Mingzhe Liu[7], Xiaoxin Zhang[1,3] , and Xueshang Feng[6]

[1]Key Laboratory of Space Weather, National Satellite Meteorological Center (National Center for Space Weather), China Meteorological Administration, Beijing, China, [2]State Key Laboratory of Space Weather, Chinese Academy of Sciences, Beijing, China, [3]Innovation Center for FengYun Meteorological Satellite (FYSIC), National Satellite Meteorological Center, China Meteorological Administration, Beijing, China, [4]Institute for the Study of Earth, Oceans, and Space, University of New Hampshire, Durham, NH, USA, [5]Climate and Space Sciences and Engineering, University of Michigan, Ann Arbor, MI, USA, [6]SIGMA Weather Group, State Key Laboratory of Space Weather, National Space Science Center, Chinese Academy of Sciences, Beijing, China, [7]LESIA, Observatoire de Paris, Université PSL, CNRS, Sorbonne Université, Université de Paris, Meudon, France

Abstract Understanding the evolution of energetic particles in the heliosphere is one of the most outstanding topics in heliophysics studies. The spectra of energetic particles are pivotal to investigate their origin, acceleration and transport processes. Using STEREO A data, we investigate an intensity enhancement of energetic ions associated with a stream interaction region (SIR) during the decay phase of a gradual solar energetic particle (SEP) event. We find the SIR has fine structures include the stream interface (SI) and a forward-reverse shock pair, and the energy spectra of energetic ion intensities show complex variations around them. Furthermore, we compare the ions' energy spectra in different regions of the SIR. The results show that this SIR is capable of accelerating protons to about 35 MeV nuc^{-1}, which is about two times of the upper limit of the energy as identified by previous observations, but they are still of the same order. We suggest this may be explained by the fact that the SIR could further accelerate the remnant lower energy ions from the gradual SEP event to higher energies. Moreover, the energetic ions in the SIR event have two populations that are accelerated by shock-associated and non-shock-associated mechanisms, respectively. In addition, the ion intensity exhibits significant directional anisotropies during this SIR event, which may be a result of the combined influence of the transport effect, shock, and the intervening small flux rope.

1. Introduction

Energetic particles with high energies could cause significant damages to both ground and space human activities (e.g., Malandraki & Crosby, 2018), therefore it is important to investigate the source, acceleration, transport and evolution of energetic particles in the interplanetary space (e.g., Desai & Giacalone, 2016; Mewaldt et al., 2012; Richardson, 2004). The energetic particle enhancements related to stream interaction regions (SIRs), namely the SIR events, have been studied for decades (e.g., Crooker et al., 1999; Mason et al., 1999; Richardson, 2004). Currently, the SIR events continually attract attention as the Parker Solar Probe and Solar Orbiter observed many SIR events in the inner heliosphere (Cohen et al., 2020; Desai et al., 2020; Joyce et al., 2020, 2021; McComas et al., 2019; Schwadron et al., 2021).

In general, SIR is formed when the trailing faster solar wind overtakes the preceding slower solar wind in interplanetary space (Jian et al., 2006; Richardson, 2018). If the SIRs are quasi-steady and recurrent structures, then this kind of compression regions is frequently referred as co-rotating interaction regions (CIRs, e.g., Belcher & Davis, 1971; Crooker et al., 1999; Huang, Liu, Klecker, & Chen, 2016; Huang, Liu, Qi, et al., 2016). The boundaries of SIRs could sometimes evolve into a pair of forward-reverse shock at several AU from the Sun (Crooker et al., 1999; Jian et al., 2006). Observational, theoretical and numerical studies suggest that SIRs could profoundly accelerate the energetic particles and also change their transport processes (e.g., Fisk & Lee, 1980; Reames, 1999; Richardson, 2004; Wu et al., 2014; Zhao et al., 2016). Most of these works relate the accelerated energetic particles to the reverse and/or forward shocks via the first order Fermi acceleration mechanism, and indicate the shocks are able to accelerate particles to several MeV nuc^{-1}, but the reverse shock is more often associated with energetic particle enhancements than forward shock (Fisk & Lee, 1980; Giacalone & Jokipii, 1997; Li, 2017; Richardson, 2004; Zhao et al., 2016). Furthermore, the compression regions without shocks are also

capable of accelerating particles to about 10 MeV nuc^{-1} with a process similar to the diffusive shock acceleration (Lee et al., 2012; Sokolov et al., 2006), and a local magnetic mirror could be a particle source for SIR events (Chotoo et al., 2000; Giacalone et al., 2002; Joyce et al., 2021; Kocharov et al., 2003; Wei et al., 2019). Richardson (2004) summarize that the SIRs/CIRs can accelerate the ions to about 20 MeV nuc^{-1} by shocks or non-shock associated mechanisms, whereas Mason et al. (2008) indicate the heavy-ion spectra could extend up to about 30 MeV nuc^{-1}. Additionally, the transport processes, including magnetic focusing or mirroring, diffusion processes, convection with solar wind, and adiabatic cooling, could also remarkably change the observational properties of energetic particles (e.g., Kocharov et al., 2009; Mason et al., 2012; Qin et al., 2006; Ruffolo, 1995; Wang et al., 2012; Zhang et al., 2009).

The energy spectra of energetic particles provide rich information regarding the processes responsible for their origin, acceleration, and transport (Mason et al., 1999; Richardson, 2004). The energy spectra associated with SIR events could be power-law or exponential forms, which are significantly different from those of typical solar energetic particle (SEP) events (Mewaldt et al., 2012; Richardson, 2004; Tylka et al., 2005). Fisk and Lee (1980) developed a model to predict the energy spectra of energetic particles associated with SIR events at 1 AU by combining the shock acceleration and the particle transport effect, resulting in softer spectrum at high energies than that at low energies and a spectrum turnover at low energies when the acceleration location is far from the observer. Some observations matched well with the model predictions, but mismatched observations were also found (Richardson, 2004). Chotoo et al. (2000) compared the spectra of two CIR events at energies from 0.52 keV nuc^{-1} to 5 MeV nuc^{-1} at 1 AU. They found the suprathermal ions between 10 keV nuc^{-1} and 500 keV nuc^{-1} peaked in intensity inside CIRs were associated with local accelerations, and the MeV nuc^{-1} intensities peaked outside the CIRs in the fast solar wind, but no turnover of spectra is observed at intermediate energies. They further concluded from the smooth transitions of ions distribution functions that the particles throughout this range should be accelerated by a single process rather than separate processes for suprathermal and MeV nuc^{-1} particles. Moreover, current observations from the Parker Solar Probe also show flat rather than rollover spectrum of low energy particles in the inner heliosphere, due to the pre-shock accelerations or sub-Parker structure of the magnetic field (Desai et al., 2020; Joyce et al., 2021; Schwadron et al., 2021). Additionally, both the theory and observations suggest that the anisotropies of particle intensities associated with SIR events are weak, due to the scattering and mirroring of the sunward propagating energetic particles (Joyce et al., 2021; Richardson, 2004).

In this work, we investigate an SIR event that appears at the decay phase of a gradual SEP event. This SIR has fine structures including one stream interface (SI) and a forward-reverse shock pair, which can directly modify the ion intensities. We find three outstanding features of this SIR event: (a) the ion intensity enhancements could approach up to about 35 MeV nuc^{-1}, (b) the spectra imply two populations of the energetic ions at low and high energies, and (c) the spectra show significant directional anisotropies. Accordingly, our analysis suggests: (a) the SIR may further accelerate the lower energy ions from the gradual SEP event to higher energies, (b) two different acceleration mechanisms work to accelerate the low and high energy ions, respectively, and (c) transport effect and other factors play a role in modifying the ion intensities along different directions and thus result in the spectral anisotropies. In Section 2, we introduce the data used in this work, and then present the observations of the SIR event and the fine structures of the SIR. In Section 3, we investigate the energy spectral differences and study the spectra variations during this SIR event. Discussion and summary are given in Section 4 and Section 5, respectively.

2. Data and Observations

2.1. Data

The Solar TErrestrial RElations Observatory (STEREO) spacecraft were launched on 2006, with STEREO A leading and STEREO B trailing the Earth, and both spacecraft orbit around the Sun at a radial distance of approximately 1 AU. The longitudinal separation between STEREO A and STEREO B increases at approximately 44°–45° per year when viewing from the Sun (Kaiser et al., 2008). The SIR event we investigate in this work was observed on 31 March 2011, when both spacecraft left the Earth for about 90° in longitudinal separation and they separated from each other for about 175.9°, indicating this event is unlikely to be observed simultaneously by multiple spacecraft.

The data used in this study are from the Plasma and Suprathermal Ion Composition (PLASTIC) experiment (Galvin et al., 2008) and the In-Situ Measurements of Particles and CME Transients (IMPACT) suite (Luhmann

et al., 2008). The solar wind plasma data, including bulk speed, solar wind proton temperature and number density, are obtained from the PLASTIC. The Magnetic Field Experiment (MAG) instrument (Acuna et al., 2008) and the Solar Wind Electron Analyzer (Sauvaud et al., 2008) onboard the IMPACT provide the magnetic field data and the suprathermal electron pitch angle distributions (PADs), respectively. The cadences of these data used in this work are 1-min. The energetic particles, including electrons, protons and minor ions, are collected by several different sensors of the IMPACT. The High Energy Telescope (HET, Von Rosenvinge et al., 2008) detects the protons from 13 to 100 MeV nuc^{-1}. The Low Energy Telescope (LET, Mewaldt et al., 2008) measures the protons over the range from about 1.8 to about 15 MeV nuc^{-1}. The Suprathermal Ion Telescope (SIT, Mason et al., 2008) provides data for protons between about 0.32 and about 3.6 MeV nuc^{-1}. The Solar Electron and Proton Telescope (SEPT, Müller-Mellin et al., 2008) records the ions from 70 to 7,000 keV nuc^{-1}. Since SEPT is not capable of elemental resolution, other species also contribute to the ion channels. In this work, we note the protons contribute predominantly to the SEPT measurements of this SIR event. Thus, in the following, we use "ion" to accurately describe the energetic particle, but we exactly mean "proton" measurements for the HET, LET and SIT observations. In addition, the SEPT and LET give measurements in different pitch angles. The time resolution of the energetic ions data used in this work is 10-min, except the cadence of HET data is 15-min.

2.2. Observations

Figure 1 shows an overview of the SIR event. The top panel (A) illustrates the differential fluxes of energetic ions observed by the sunward telescope of the SEPT, indicating the SIR event as marked by the shaded region was preceded by a gradual SEP event, which has been well studied by several works (Mewaldt et al., 2013; Ng, 2014; Park et al., 2013; Richardson et al., 2014; Rouillard et al., 2012). During this SIR event, the sunward telescope of SEPT looks to the sunward direction that detects the anti-sunward streaming ions, whereas the anti-sunward telescope measures the sunward streaming ions from the anti-sunward direction. In order to avoid confusion, we hereafter use the sunward and anti-sunward streaming ions to represent the ions observed by the anti-sunward and sunward telescopes of the SEPT, respectively.

In this work, we focus on the SIR event in the decay phase of the gradual SEP event, and the associated energetic ion enhancements are observed between 06:06 UT on March 30 and 12:37 UT on March 31. Furthermore, the effects of background and preceding event are predicted in different energy channels, as shown by the three dashed lines in panel (A). For the calculations, we choose the ion intensities in each energy channel between March 27 and March 30 to fit their decay trends with an exponential function, and we then extend the fittings to the SIR and beyond regions from March 30 to April 2 as the expected intensities of the background and preceding event. The comparisons also suggest the ion intensities in the SIR region are much higher than the predictions, and the ion intensities in the leading and trailing SIR regions also slightly increase as compared with predictions, implying the ions are accelerated around the SIR. Panels (B) to (H) present the details of this SIR event. Panel (B) exhibits the solar wind proton number density variations of the SIR. Panels (C) to (G) show the ion intensities at different energies with measurements obtained from the HET, LET, SIT, the sunward and anti-sunward telescopes of the SEPT, respectively. The bottom panel indicates the intensity anisotropies of anti-sunward to sunward streaming ions. The shaded regions in this figure mark the SIR, with the gold vertical lines showing the boundaries, which are forward shock (FS) and reverse shock (RS). The vertical black line suggests the position of the SI at 16:10 UT on March 30. The blue and red vertical dashed lines mark four boundaries of the interested regions that we will discuss later.

The fine structures of the SIR are presented in Figure 2. From top to bottom, the panels show the suprathermal electron PADs at energy of 246.8 eV, the magnetic field components in RTN coordinates, the azimuthal angle ϕ_B, the solar wind proton number density N_p, bulk speed V_p, proton temperature T_p, East-West flow angle, and the specific entropy argument $S = T_p/N_p^{2/3}$. The shaded region and the vertical lines have the same meanings as those in Figure 1. We can see the magnetic field strength $|B|$, the N_p, V_p, and T_p all show a jump at the boundaries of the shaded region, with the jumps at the trailing side are slightly more significant than that at the leading side, implying this is a forward-reverse shock pair with the forward shock at 06:06 UT on March 30 and the reverse shock at 12:37 UT on March 31. In general, the SI is identified by several signatures (Crooker et al., 1999), including the standard criteria (decreasing N_p, increasing T_p, and a flow shear), the compositional characteristics (increasing alpha to proton abundance, decreasing freezing-in temperatures and first-ionization-potential elemental abundance ratios, and onset of alpha-proton differential speed), and some additional criteria (peak in total
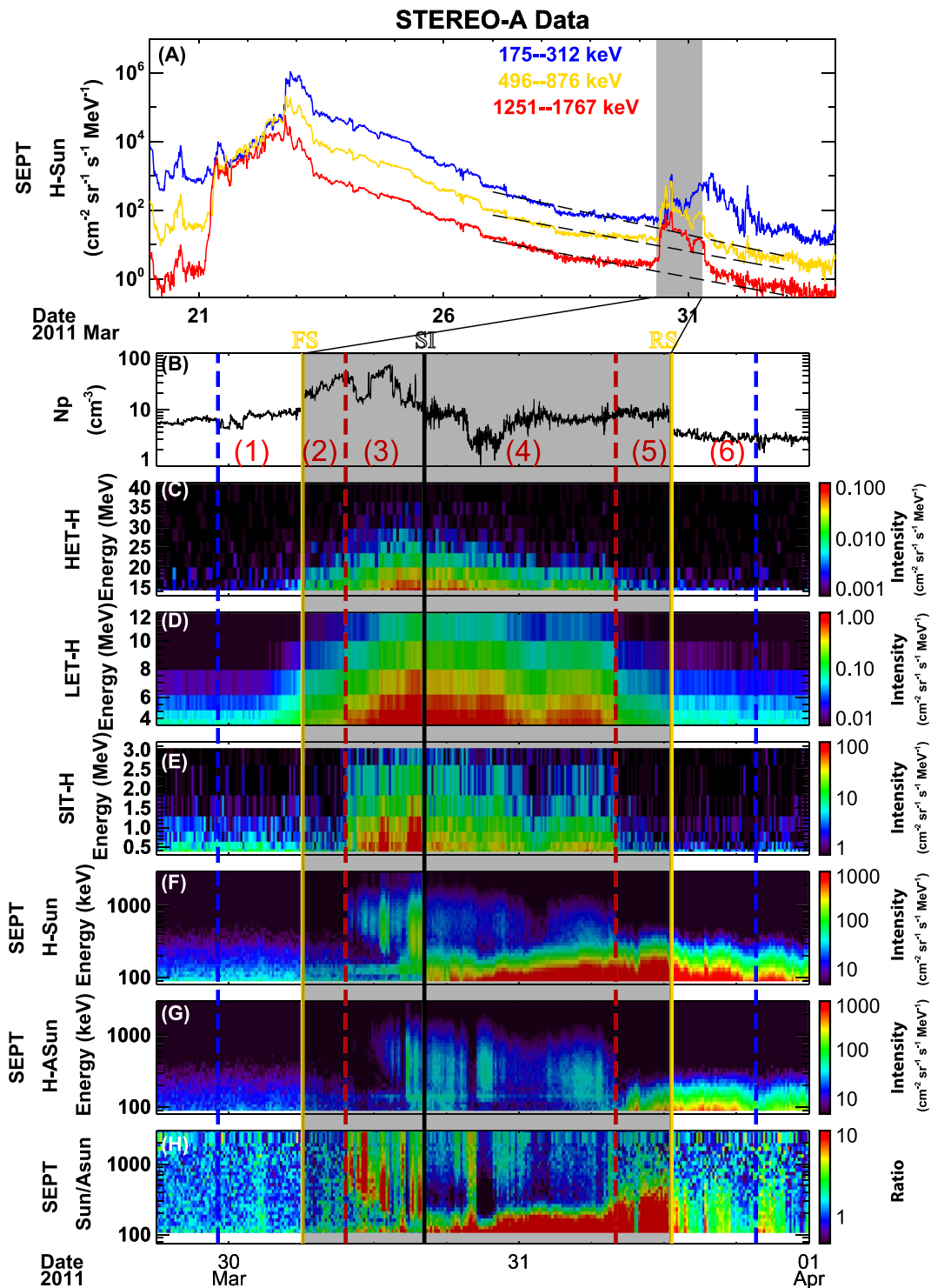
Figure 1. Overview of the SIR event. Panel (a) shows the ion intensities in three energy bands measured by the sunward telescope of SEPT instrument between 2011 March 20–2011 April 3. The shaded region indicates the stream interaction region (SIR). The three dashed lines exhibit the expected intensities in the SIR and beyond. Panel (b) shows the solar wind proton number density. From panel (c) to panel (g), the ion intensities measured by the HET, LET, SIT, the sunward and anti-sunward telescopes of SEPT are presented, respectively, and the unit of the differential fluxes is cm^{-2} sr^{-1} s^{-1} MeV^{-1}. The bottom panel (h) presents the intensity anisotropies of the ions observed by the sunward and the anti-sunward telescopes of SEPT. The shaded regions mark the SIR, with the gold vertical lines showing the boundaries, which are forward shock (FS) and reverse shock (RS). The black vertical line indicates the stream interface (SI). The blue (23:06 UT on March 29 and 08:02 UT on March 31) and red (09:40 UT on March 30 and 19:37 UT on March 31) vertical dashed lines mark four boundaries of the targeted regions, see details in the text. The colors in panels (c) to (g) indicate the ion intensities, and the colors in the last panel mean the ratios of the sunward to the anti-sunward intensities.
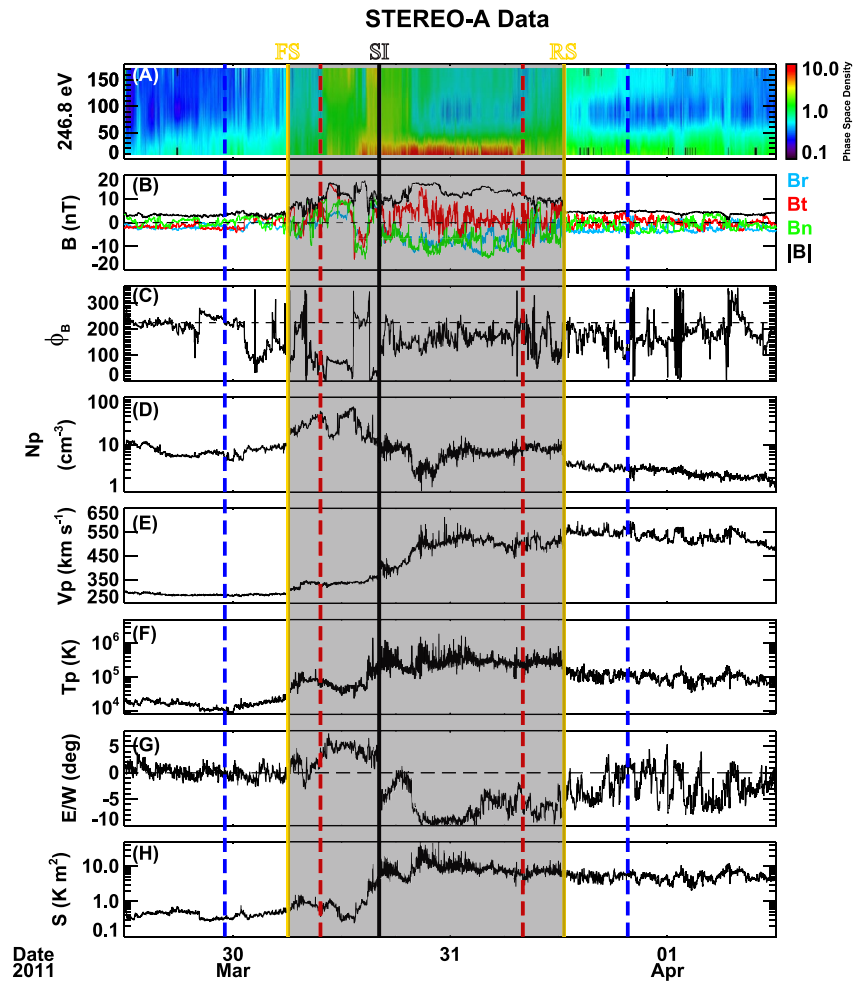
Figure 2. Overview of the SIR structure. From top to bottom, the panels show the suprathermal electron pitch angle distributions at energy of 246.8 eV, the magnetic field components in RTN coordinates, the azimuthal angle ϕ_B, the solar wind proton number density N_p, bulk speed V_p, proton temperature T_p, East-West flow angle, and the specific entropy argument S. The colors in panel (A) represent the phase space density of electrons, and the unit is kg^{-3} s^3 m^{-6}. The shaded region and the vertical lines have the same meanings as those in Figure 1.

pressure, magnetic field discontinuity). Based on these requirements, the SI of this SIR is located at 16:10 UT on March 30 as indicated by the black vertical line, when the proton density decreases, the proton temperature increases, and a significant East-West velocity shear appears at the crossing. We note that this SIR and the reverse shock are listed in two online catalogs (Jian et al., 2013), but the forward shock is not included. In addition, we find that there were no eruptions based on the remote-sensing observations or large interplanetary structures based on the in-situ observations during this energetic ion enhancements, indicating that the compression region is solely responsible to the ion enhancements.

Moreover, several characteristics of this SIR event are indicated by Figure 1:

1. The intensity enhancements of energetic ions could extend to energies up to about 35 MeV nuc^{-1}. Previous studies found the SIRs/CIRs could accelerate ions to several MeV nuc^{-1} in the mid-distance heliosphere near the solar minimum (Balogh et al., 1999; Gómez-Herrero et al., 2010) and up to about 20 MeV nuc^{-1} as summarized by Richardson (2004), and the heavy-ions spectra could extend up to about 30 MeV nuc^{-1} (Mason et al., 2008). However, the HET observations in panel (C) demonstrate evidential proton enhancements to nearly 35 MeV nuc^{-1}, which is about two times of the previous observations (Richardson, 2004), implying the SIR is capable of accelerating the protons to higher energies. Furthermore, we also find several SIR events with similar plasma properties to our SIR but without a preceding SEP event, and we find the ion enhancements in these SIR events are similar to previous results that the ions cannot exceed energies

of 20 MeV nuc^{-1}. Thus, the preceding gradual SEP event in our SIR event implies that the SEP event may provide seed ions for further acceleration by the SIRs. However, other factors may also contribute, which may need to combine the models and the observations to investigate the contributions of different factors. We also note that the ion intensities around the SI are slightly different (also refer to Figure A1), and the asymmetry as shown in panels (C) to (H) is caused by the SI due to it is a tangential discontinuity that separate two different solar wind regimes, which could prevent the free transport of energetic ions(Richardson, 2004).

2. The energetic ions in the SIR event have two populations. Panels (F) and (G) indicate the ion intensities at energies higher than about 300 keV nuc^{-1} are somewhat similar in both sunward and anti-sunward directions, and their distributions between the red lines are comparable to the higher energy ions detected by the HET, LET and SIT telescopes as shown in panels (C) to (E), with all the intensities peaking at around the SI (also refer to Figure A1). This suggests the ions at relatively higher energies observed by the SEPT have similar characteristics with that observed by the HET, LET and SIT. Furthermore, after the SI, the anti-sunward streaming ions at relatively lower energies (<300 keV nuc^{-1}) are widely enhanced from the SI to beyond the reverse shock, whereas the sunward streaming ions are predominately increased in limited regions around the reverse shock. However, the intensities of lower energy ions in both directions peak at the reverse shock (also see panels (F) and (G) in Figure A1), implying the lower energetic ions (<300 keV nuc^{-1}) are different from the higher energy ones. Therefore, the energetic ions in this SIR event have two populations, with one population peaking in intensity around the SI while the other one peaking at the RS.

3. Panel (H) indicates remarkable anisotropies of ion intensities between the anti-sunward and sunward streaming ions. The anti-sunward streaming ions are much higher than the sunward streaming ones at relatively higher energies (>300 keV nuc^{-1}) before the SI, but these ions are dominant at relatively lower energies (<300 keV nuc^{-1}) after the SI. In other regions, the anisotropies of ion intensities are much weaker. The similar feature is also captured by the LET, which provides measurements in 16 sectored looking directions at high energy channel (HI, 6–10 MeV), low energy channel (LO, 4–6 MeV), and very low energy channel (VLO, 1.8–3.6 MeV), respectively, as shown in the supplementary Figure A2 and the description in the appendix. Therefore, the large directional anisotropies in the SIR event is distinct. We will try to discuss the contributions of the SIR fine structures and the related transport effects and/or acceleration mechanisms in following sections.

3. Energy Spectral Variations

In this section, we will discuss the energy spectral variations of the energetic ions outside and inside the SIR.

In order to study the spectral variations, we choose several regions for further comparisons. As shown in Figure 1, region (1) is from the blue line to the leading edge of the SIR, which indicates the ion performance before the SIR event. The region trailing the SIR until the trailing blue line is marked as region (6). Regions (3) and (4) indicate the regions before and after the SI, respectively, and they are selected to be consistent with the enhancements of the ion intensities at energies between 1 and 3 MeV observed by SEPT and SIT. The leading edge of the SIR to the leading red line is region (2), while region (5) is from the trailing red line to the trailing edge of the SIR, and the high energy ions are not significantly increased in these two regions as compared with that in regions (3) and (4). The durations of regions (1) and (6) are selected to be comparable to the regions identified inside the SIR, and we use the averaged ion intensity in each region to remove the influence of different durations of the selected regions. In this following, we analyze the spectral variations of the energetic ions in details.

3.1. Spectra Outside the SIR

At the beginning, we would like to discuss the spectral signatures outside the SIR. Figure 3 shows the ion average intensity with measurement uncertainty as a function of energy in regions (1) (black squares) and (6) (red filled squares). Panels (A) and (B) present the same observations from both the LET and the HET, but show the ion measurements of anti-sunward and sunward streaming ions from the sunward and anti-sunward telescopes of SEPT, respectively. Here, we use the unsectored proton intensities from LET, because the sectored LET observations only include three energy channels, which is not good enough to fit the energy spectra as compared with the unsectored proton intensities in 12 energy channels. In addition, the SIT observations are not used because its energy range is overlapped by SEPT (lower energy) and LET (higher energy). When calculating the averaged ion intensities, we have removed the background and pre-event effects with the method stated above. The first two
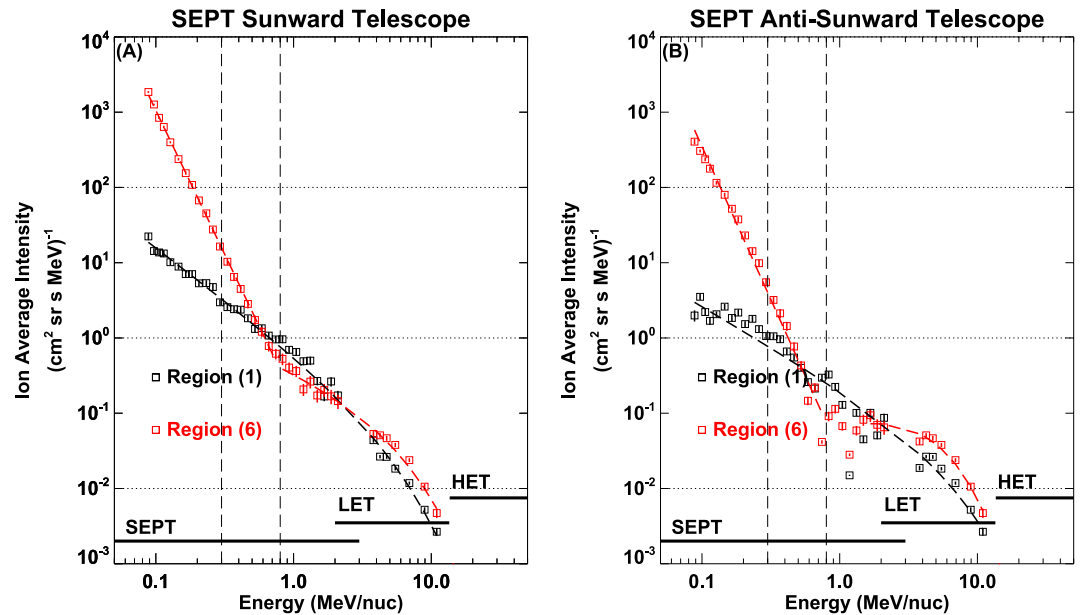
Figure 3. The energy spectra variations outside the SIR event. The two figures present the ion average intensity as a function of energy with the measurements from the SEPT, LET and HET. The measurements from the sunward and anti-sunward telescope of SEPT are used in Panel (a) and Panel (b), respectively. The energy spectra in regions (1) and (6) are illustrated with black and red colors, respectively, with the fittings overlapped. The measurement uncertainties are also added. The fitting methods and parameters are presented in Table 1. The two vertical dashed lines indicate the energies at 0.3 MeV nuc^{-1} and 0.8 MeV nuc^{-1}, respectively. The horizontal black bars at the bottom mark the available energy bands of the SEPT, LET and HET. The background and pre-event intensities are subtracted in the calculations of ion average intensities.

channels of SEPT are excluded as suggested by SEPT Caveats (http://stereo.ssl.berkeley.edu/SEPT_Caveat.pdf), and the negative or unavailable values are removed from the figures.

Furthermore, we fit the spectra in both regions either with a simple power-law function ($j = j_0 E^{-\gamma}$) or a power-law with an exponential rollover function (i.e., Ellison-Ramaty function (Ellison & Ramaty, 1985)) in the form of $j = j_0 E^{-\gamma} EXP(-E/E_0)$, where j is the ion average intensity at energy E, j_0 is the normalization constant, γ is the power-law spectral index, and E_0 is the e-folding energy (Desai et al., 2020; Jones & Ellison, 1991; Joyce et al., 2021). We do the power-law fittings with *LINFIT* function of IDL, and we perform the later form of fittings by minimizing the χ^2 value with the implementation of a nonlinear least-squares Levenberg-Marquardt technique in the *MPFITFUN* module for IDL (Markwardt, 2009). We also perform the fittings in the four regions inside the SIR. The fitting methods, the parameters, and the reduced-χ^2 (χ_ν^2) are given in Table 1. In regions (1) and (3), the spectrum in each region is fitted with the Ellison-Ramaty function. In regions (2) and (4)–(6), the spectrum in each region is fitted in two parts that divided by a separation energy, due to the power-law signature of the spectrum at low energies. Thus, the spectrum is fitted with the power-law function at low energies, whereas the Ellison-Ramaty function is used at high energies. Additionally, we also use the generalized pan-spectrum formula (Liu et al., 2020), which incorporates the power-law, Ellison-Ramaty, Kappa, Maxwellian, and logarithmic-parabola functions to self-consistently determine the spectral features of energy particles, to fit the energy spectra of our event. We find our results match well with that derived by pan-spectrum technique when the single power-law or Ellison-Ramaty function is determined as we do. But pan-spectrum technique also determines other functions as the best fittings, which is not reasonable in the same event but reflects the complications of energy spectral variations. Thus, we focus on our fittings in the following analysis.

From Figure 3, it is clear to see the energy spectra show significant differences before and after the SIR event. As shown in Figure 3a, the spectrum in region (1) is well fitted by the Ellison-Ramaty function. However, the spectrum in region (6) is divided into two parts with the energy that separates at about 0.8 MeV nuc^{-1}. In general, the break energies are determined by the acceleration mechanism, and the spectral indices below the break energy are also related to the accelerations (Joyce et al., 2021; Richardson, 2004). Therefore, the well fitted power-law function below 0.8 MeV nuc^{-1} implies that these ions should be accelerated by the reverse shock, which is

Table 1
Fitting Parameters for the Spectra of Energetic Ions in the Six Regions

Regions	Sunward Telescope of SEPT				Anti-Sunward Telescope of SEPT			
	j_0	γ	E_0	χ_ν^2	j_0	γ	E_0	χ_ν^2
(1)	0.66 ± 0.05	1.38 ± 0.05	4.71 ± 0.59	0.65	0.22 ± 0.02	1.07 ± 0.05	6.15 ± 1.01	2.09
(2) (<0.8 MeV)	0.46 ± 1.09	1.58 ± 0.06	N/A	0.09	0.04 ± 1.77	1.87 ± 0.35	N/A	2.76
(2) (>0.8 MeV)	0.89 ± 0.06	0.70 ± 0.08	5.26 ± 0.26	2.59	0.36 ± 0.03	0.11 ± 0.08	4.37 ± 0.19	3.90
(3) (>0.8 MeV)	$3.05 \times 10^1 \pm 2.30$	1.91 ± 0.07	8.13 ± 0.39	1.03	9.89 ± 0.73	1.29 ± 0.07	6.62 ± 0.27	0.69
(4) (<0.3 MeV)	0.09 ± 1.13	4.21 ± 0.07	N/A	0.01				
(4) (>0.3 MeV)	8.24 ± 0.38	1.00 ± 0.04	4.56 ± 0.13	1.98	8.31 ± 0.37	1.12 ± 0.05	4.89 ± 0.15	1.28
(5) (<0.8 MeV)	0.34 ± 1.11	4.02 ± 0.07	N/A	0.13	0.07 ± 1.18	3.29 ± 0.11	N/A	0.35
(5) (>0.8 MeV)	1.27 ± 0.10	0.76 ± 0.14	3.00 ± 0.23	1.43	0.54 ± 0.04	-0.02 ± 0.14	2.40 ± 0.15	1.49
(6) (<0.8 MeV)	0.16 ± 1.04	3.82 ± 0.03	N/A	0.02	0.03 ± 1.19	4.06 ± 0.11	N/A	0.37
(6) (>0.8 MeV)	0.40 ± 0.03	0.76 ± 0.20	4.37 ± 1.00	0.69	0.10 ± 0.02	-0.77 ± 0.39	2.26 ± 0.40	0.50

Note. In regions (1) and (3), the spectrum in each region is fitted with a power-law with an exponential rollover function (i.e., Ellison-Ramaty function) in the form of $j = j_0 E^{-\gamma} EXP(-E/E_0)$, where j is the ion average intensity at energy E, j_0 is the normalization constant, γ is the power-law spectral index, and E_0 is the e-folding energy. In regions (2) and (4)–(6), the spectrum in each region is fitted in two parts, with the separation energy presenting in the bracket. In the high energy band, the fitting function is the same to that assembled in regions (1) and (3). In the low energy band, the spectrum is fitted with a simple power-law function $j = j_0 E^{-\gamma}$, thus the e-folding energy E_0 in the exponential rollover function is not available in these fittings. In region (4), the energy spectrum of the ions from anti-sunward direction does not show a simple power-law in low energy band (<0.3 MeV nuc^{-1}), thus no fitting is available.

consistent with the results that the reverse shock of SIRs could accelerate sub-MeV ions (Fisk & Lee, 1980; Li, 2017; Zhao et al., 2016). Figure 3b shows similar results of the sunward streaming ions, except that the spectrum above the separation energy is scattering due to low intensities. As shown in Table 1, the γ in both directions are very similar in region (1) (1.38 ± 0.05 vs. 1.07 ± 0.05) and in region (6) below 0.8 MeV nuc^{-1} (3.82 ± 0.03 vs. 4.06 ± 0.11). In general, when fitting the energy spectra with a power-law function at 1 AU, the γ indices are about 4.0 above 1.0 MeV nuc^{-1} and about 2.0 below 1.0 MeV nuc^{-1} in SIR/CIR events (e.g., Cohen et al., 2020; Richardson, 2004). Thus, the larger γ of the spectra below 0.8 MeV nuc^{-1} in region (6) reflects this reverse shock is less efficient to accelerate these ions, but the inefficiency could be balanced as the ions from the gradual SEP event may act as a role of seed ions for further accelerations and these ions already have some energies.

3.2. Spectra Inside the SIR

Figure 4 shows the energy spectra in the four regions (as shown by the legend) inside the SIR. Similar to Figure 3, Figure 4a and Figure 4b exhibit anti-sunward and sunward streaming ions measured by SEPT, respectively. The black triangles, light blue triangles, red circles and blue circles represent the energy spectra with measurement uncertainties in region (2) to region (5). We can also see the energy spectra extend to about 35 MeV nuc^{-1}, and they show remarkable changes in different energies, different directions, and also different regions of the SIR.

From Figure 4, we can see the spectra in regions (2) and (5) are much different from those in regions (3) and (4). At the beginning, we would like to investigate the spectra in regions (2) and (5). In both regions, the spectra are well fitted in two parts with the energy separates at about 0.8 MeV nuc^{-1}, as shown by the figure and Table 1. Above 0.8 MeV nuc^{-1}, the γ is similar between region (2) and (5) in the same direction. However, due to the high energy ions above 0.8 MeV nuc^{-1} are not significantly increased in the two regions and the fitting results are predominantly deviated by the several scattering data points near the separation energy, we will focus on the low energy ions. Below 0.8 MeV nuc^{-1}, the γ in both directions are comparable in region (2) (1.58 ± 0.06 vs. 1.87 ± 0.35) and in region (5) (4.02 ± 0.07 vs. 3.29 ± 0.11). The γ further indicates that the ions are less efficiently accelerated in region (5) than that in region (2), but the ion average intensities are more profound in region (5) than that in region (2). Moreover, the two-part fitting in region (2) also implies the forward shock works to accelerate ions at low energies, though this signature is not outstanding in Figure 1. As introduced above, previous results suggest that the reverse shock is more often associated with ion enhancements (Richardson, 2004), because the reverse shock could be more efficient at accelerating pickup ions than forward shock (Giacalone
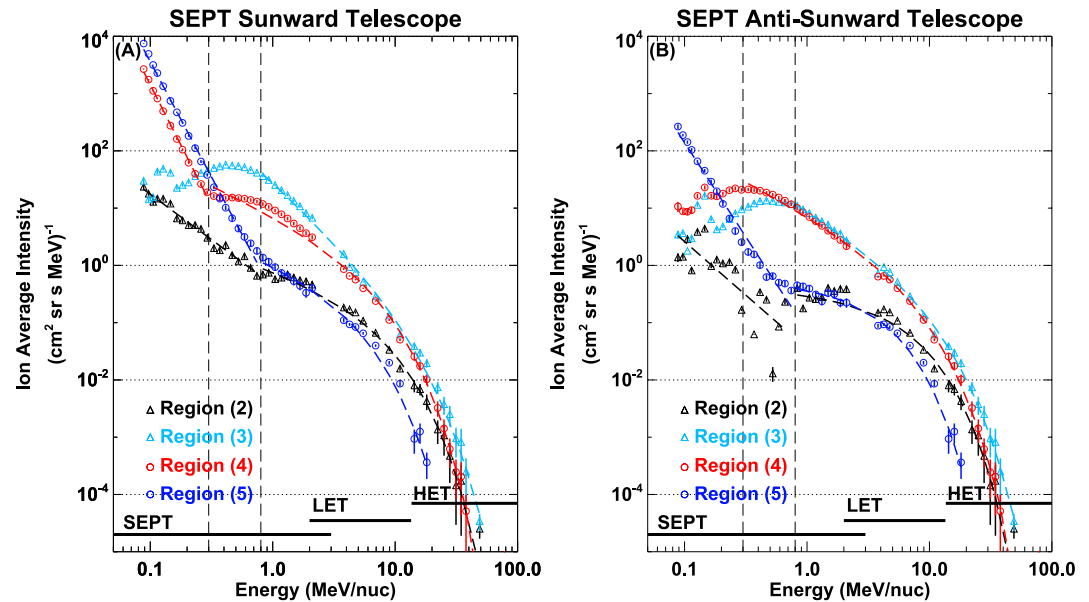
Figure 4. The energy spectra variations inside the SIR event, with similar format to Figure 3. The different colored symbols indicate the ion average intensities with measurement uncertainties in different regions inside the SIR, as suggested by the legend.

& Jokipii, 1997; Gómez-Herrero et al., 2009). However, in this event, the less efficient accelerations of the reverse shock may be a result of the smaller Alfvénic Mach number of reverse shock as discussed in Section 4.1, whereas the more profound intensity enhancements in region (5) could be caused by the better connection with the observer for the reverse shock and the longer duration of region (5). We also note the fittings below 0.8 MeV nuc^{-1} are very close in region (5) and region (6) in both directions, indicating the low energy ions in both regions should from the same source, that is, the reverse shock. If we fit the spectra under 0.8 MeV nuc^{-1} in region (1) with power-law function, the γ would be 1.41 ± 0.03 ($j_0 = 0.61 \pm 1.06$, $\chi_\nu^2 = 0.04$) for anti-sunward streaming ions and 1.13 ± 0.11 ($j_0 = 0.22 \pm 1.18$, $\chi_\nu^2 = 0.34$) for sunward streaming ions, respectively. The results are also very similar to that in region (2), implying the low energy ions in regions (1) and (2) could be accelerated by the forward shock.

The spectra around the SI show much different characteristics. First, the spectra indicate turnover signature at low energies. Except the spectrum of anti-sunward streaming ions in region (4) as shown in Figure 4a, the spectra in regions (3) and (4) exhibit clear turnover signature even though the data points are somewhat scattering at low energies. Second, the steepened spectrum of the anti-sunward streaming ions in region (4) at low energies (<0.3 MeV nuc^{-1}) should be caused by the reverse shock. This is evidential because the power-law index (4.21 ± 0.07) is close to that in regions (5) and (6) as shown in Table 1, and these ions decrease from the reverse shock to the SI as shown in panel (F) of Figure 1 and Figure A1, indicating the perpendicular diffusion of the low energy ions between the SI and the reverse shock (Dwyer et al., 1997; Intriligator et al., 2001). The spectra in region (3) do not steepen because the forward shock may not be capable of accelerating substantial ions, and the ions accelerated by the reverse shock could not cross the SI, which is more prominent to prevent low energy ions due to their small gyro-radius. Third, the spectral anisotropies are profound between sunward and anti-sunward directions. The anti-sunward streaming ion intensities are much higher than the sunward streaming ion intensities at energies above 0.3 MeV nuc^{-1} in region (3) and at energies below 0.3 MeV nuc^{-1} in regions (4) and (5). Besides, the sunward streaming ions under 0.3 MeV nuc^{-1} cannot penetrate into the region (4), which is much different from the anti-sunward streaming ions in the same region. We will be discuss the spectral directional anisotropies in the following section.

4. Discussion

4.1. Two Acceleration Mechanisms

The two populations of low and high energy ions in the SIR event indicate they are accelerated by different mechanisms. As stated above, the low energy ions below 0.8 MeV nuc^{-1} are locally accelerated by the forward-reverse shock pair. However, the high energy ions should be accelerated by non-shock associated mechanisms.

In general, the ion enhancements in SIR events have several different distributions (e.g., Richardson, 2004, and references therein): (a) the ions distribute around the shock locally, which indicates typical shock accelerations; (b) the ion enhancement peaks at the shock and decreases to the SI, which implies shock accelerations together with perpendicular diffusion of the ions; (c) the ions increase locally around the SI, which suggests non-shock associated accelerations. Additionally, the SIRs/CIRs without shocks can also accelerate ions via a process similar to the diffusive shock acceleration and/or transport processes such as magnetic focusing effect, which could lead to ion enhancements inside the whole compression regions (Giacalone et al., 2002; Kocharov et al., 2003; Wei et al., 2019).

From Figure 1 and Figure A1, we can see the high energy ions distribute primarily in regions (3) and (4), and the ion intensities nearly peak at the SI. Consequently, if the ions around the SI are accelerated by the remote shocks as suggested by Fisk and Lee (1980), then the ion enhancements should peak at around the shock and decrease from the boundary to the SI through perpendicular diffusion (Dwyer et al., 1997; Intriligator et al., 2001). But the ion enhancements in regions (3) and (4) both peak at the SI and decrease reversely from the SI to the boundaries. This implies that these ions are accelerated through non-shock associated mechanisms. But the actual mechanisms are not clear, it could be one or a combination of several acceleration mechanisms including the statistical acceleration (Schwadron et al., 1996), compressions through a process similar to the diffusive shock acceleration (Chotoo et al., 2000; Giacalone et al., 2002; Kocharov et al., 2003), and other non-shock accelerations.

We note the high energy ion intensities in regions (2) and (5) are remarkably reduced in comparison with that in regions (3) and (4), which could be caused by two reasons. On one hand, this could be a natural consequence of the decayed intensities from the SI to the SIR boundaries. As shown in Figures 3 and Figure 4, we can see the reduced high energy ions in these regions are still more profound than that outside the SIR in regions (1) and (6). On the other hand, the magnetic focusing effect may contribute. As suggested by the simulation results of Wei et al. (2019), the magnetic focusing effect could modify the ion intensities in compression regions. The ions are trapped by the compression region and are reflected back and forth by mirror points that close to the Sun and that at large heliocentric distances. However, the magnetic focusing is effective when the reciprocal value of magnetic focusing length $\left(L_B^{-1}\right)$ is small. But the magnetic focusing length L_B is not uniformly changing in the compression region, and the L_B at the edges is usually too small to reflect the ions effectively. Therefore, the predominant ion enhancements are in the center of the compression regions.

In addition, we discuss the possible acceleration mechanisms of the forward-reverse shock pair. According to the theories, the first-order Fermi acceleration (FFA) predicts power-law index $\gamma \sim (r + 2)/(2r - 2)$ based on the spectrum of ion differential intensity versus energy $j \sim E^{-\gamma}$ (Drury, 1983; Lee et al., 2012), where r is the density compression ratio. Yang et al. (2019) find the protons between 0.2 and 1 MeV are mostly accelerated via shock drift acceleration (SDA) at both quasi-parallel and quasi-perpendicular shocks. Moreover, the FFA and SDA can work together under the theory of diffusive shock acceleration (DSA) (Desai & Giacalone, 2016; Lee et al., 2012; Schure et al., 2012; Yang et al., 2019; Zank et al., 2015). For the forward shock, we find the shock normal is $[-0.966, -0.188, -0.178]$, shock speed V_{sh} is 319.7 km/s, the angle between the shock's normal and upstream magnetic field θ_{Bn} is 64.97°, magnetosonic Mach number M_s is 17.70, Alfvénic Mach number M_A is 11.63, the density compression ratio r_{Np} is 2.04, and magnetic compression ratio r_B is 1.70. For the reverse shock, the shock normal is $[-0.722, -0.632, -0.281]$, V_{sh} is 269.7 km/s, θ_{Bn} is 16.21°, M_s is 5.89, M_A is 5.52, r_{Np} is 2.04, and r_B is 1.99. Therefore, this forward shock is a quasi-perpendicular shock with high M_A, whereas this reverse shock is a quasi-parallel shock with the same density compression ratio as the forward shock. For the forward quasi-perpendicular shock, γ is predicted to be 3.89 by FFA. But the fitted power law indices in regions (1) and (2) is between 1.07 and 1.87, which are not consistent with the prediction. In addition, Gómez-Herrero et al. (2009) investigate the CIR-accelerated ions observed by STEREO SEPT through 13 Carrington rotations, they find the spectral indices are typically near 2.7 and the spectrum shows a progressive flattening at lower energies, with the spectrum index being 2.02 ± 0.03 for ions between 220 and 876 keV, but the exact acceleration mechanisms
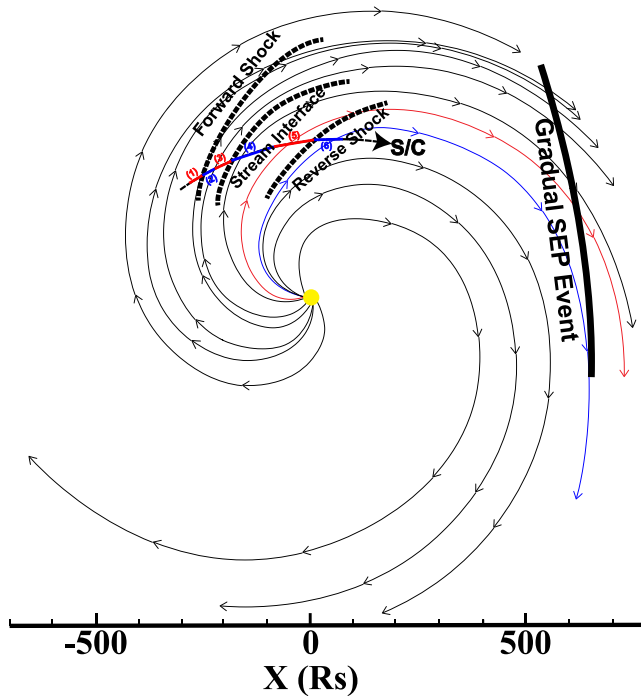
Figure 5. The sketch of the SIR. The solid lines indicate the magnetic field lines, and the dashed line with bold arrow represents the spacecraft (S/C) trajectory. The three bold dashed lines suggest the forward shock, stream interface, and reverse shock, respectively. The red and blue colors mark the six regions of this SIR event. The estimated position of the gradual SEP event is also marked.

are still not well known. Thus, the spectra index of this event is very close to the typical index of CIR/SIR events, but the flatter index indicates other mechanisms, for example, the SDA and DSA, may involve with the acceleration processes at the forward shock. For the reverse quasi-parallel shock, the predicted γ are the same to that for the forward shock as they have the same r_{Np}. Since the fitted power law indices in regions (4) to (6) are around 4, they match pretty well with FFA prediction, which is also consistent with the fact that FFA is thought to be more efficient under parallel/quasi-parallel shock geometries. Consequently, the ions are accelerated by FFA at the reverse shock. As a result, we suggest the ions are accelerated by FFA mechanism at reverse shock, but the SDA along with other mechanisms may contribute to acceleration processes at the forward shock.

4.2. Spectral Anisotropies

The SIR events usually show weak directional anisotropic spectra (Joyce et al., 2021; Richardson, 2004; Richardson, 2018). In this SIR event, the spectra in regions (1), (2) and (6) are similar in both directions, but significant spectral anisotropies are observed mainly in regions (3) to (5). As summarized in Section 2.2 and Section 3, the anti-sunward streaming ions dominate at energies above 0.3 MeV nuc^{-1} in region (3) before the SI but dominate at energies below 0.3 MeV nuc^{-1} in regions (4) and (5) after the SI, and the sunward streaming ions under 0.3 MeV nuc^{-1} cannot transport into region (4). We suppose the spectral anisotropies between the sunward and anti-sunward streaming ions may be caused by several reasons.

First, the directional spectral anisotropies at energies below 0.3 MeV nuc^{-1} in regions (4) and (5) could be a result of the magnetic connection with the shock and the transport effects. As analyzed above, the low energy ions are accelerated by the reverse shock. Therefore, magnetic connections between

the observer and the shock could significantly change the ions distribution. Figure 5 presents a sketch of the SIR event in this work. The solid lines represent the magnetic field lines, the bold dashed lines show the fine structures of the SIR, and the dashed line with arrow indicates the spacecraft (S/C) trajectory with the six regions marked approximately. The estimated position (~3 AU) of the gradual SEP event is also marked, which also indicates the seed ions from the gradual SEP event could contribute to the SIR event through the magnetic field connections. As shown by red and blue lines in the sketch, the magnetic field lines may connect the observer with the shock on the sunward parts, then the predominant anti-sunward streaming ions are expected in regions (4) and (5). The magnetic connections between the shock and the observer could be a reason of the weak directional anisotropies in other regions. Another explanation of the anisotropy could be the transport effects. As described above, the ions are reflected forward and backward in the SIR by the mirror points that are close to the Sun and that at large heliocentric distances (Giacalone et al., 2002; Kocharov et al., 2003; Wei et al., 2019). When the low energy ions propagate to the mirror points at large radial distances, they may be randomly scattered away, and some of the reflected low energy ions may not be able to reach the observer due to adiabatic deceleration if the mirror points are sufficiently far from the observer (Fisk & Lee, 1980). Thus, the sunward streaming ions could be heavily reduced in these regions.

Second, the sunward streaming ions under 0.3 MeV nuc^{-1} could not transport into region (4) may relate to the magnetic turbulence around the reverse shock. In general, we should see both anti-sunward and sunward streaming ions around the reverse shock, and the accelerated ions should decrease from the shock to farther places. Therefore, it is anticipated to see similar sunward streaming low energy ions as that of the anti-sunward streaming ones in region (4), even though they could be heavily reduced due to the decayed intensities from the shock to the SI, the magnetic connections, and the mirroring effect as analyzed above. But the flat spectrum of the sunward streaming ions indicates that these ions are constrained in a limited region around the shock. We note that the first-order Fermi acceleration at the reverse shock also relies on the magnetic turbulence to scatter ions back and forth across the shock (Zank et al., 2015). Thus, if there is no enough turbulence to scatter the ions
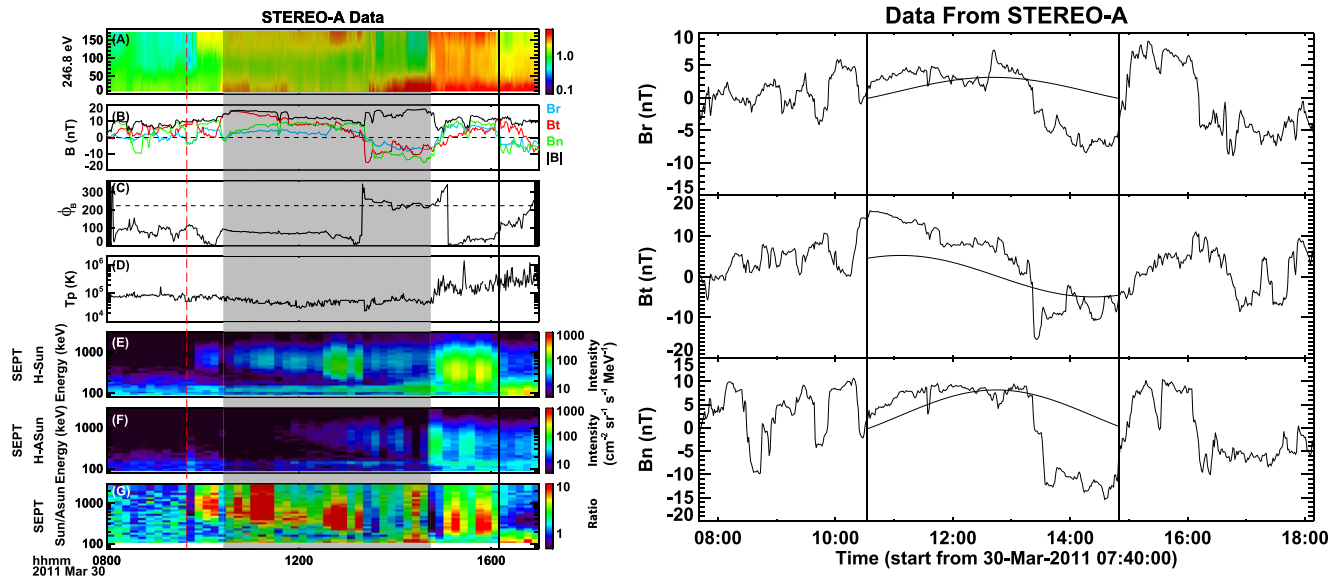
Figure 6. The small flux rope in region (3). The left figure shows the STEREO-A observations. From top to bottom, the panels show the suprathermal electrons pitch angle distributions, the magnetic field components, the azimuthal angle, the proton temperature, the intensities of anti-sunward and sunward streaming ions, and the intensity anisotropies between the two directions. The red and black lines mark the region (3) as that in Figure 1 and Figure 2. The shaded region marks a small flux rope. The right figure shows the Lundquist fitting result of this small flux rope.

back to the shock front, or the turbulence is weak to trap the ions that leads the insufficiently accelerated ions decrease strongly with distance from the shock, then the sunward streaming ions may only appear in a limited region around the shock and could not transport far away from the shock front. However, we note that the decayed intensities from the shock to the SI, the magnetic connections, and the mirroring effect may work together with the turbulence to regulate the sunward streaming ions.

Third, the dominant anti-sunward streaming ions above 0.3 MeV nuc^{-1} in regions (3) implies extra local accelerations of ions possibly by an intervening small flux rope. The left figure in Figure 6 presents the zoom-in figure of the region (3) with the panels same to that in Figures 1 and Figure 2. Panel (G) in this figure suggests the anti-sunward streaming ions are further enhanced as compared with the sunward streaming ones, implying the anti-sunward streaming ions could be further accelerated. However, they are unlikely to be accelerated remotely. If so, it is expected to see the anisotropies of the ions above 0.3 MeV nuc^{-1} in both region (3) and region (4), because the ions in both regions are accelerated through similar processes from the above analysis. But these ions are nearly isotropic in region (4). Therefore, the anti-sunward streaming ions in region (3) should be further modified locally. In addition, studies suggest that the local ion accelerations may relate to turbulence and local structures such as the small flux rope and heliospheric current sheet (Le Roux et al., 2015; Zank et al., 2015; Zharkova & Khabarova, 2012). A current study of Zhao et al. (2019) indicates that the turbulence, heliospheric current sheet, and small flux ropes at 5 AU are favorable for extra ion accelerations in local position. In Figure 6, the shaded region indicates a small flux rope structure that characterized by the smooth rotations of magnetic components and the azimuthal angle ϕ_B, the enhanced magnetic field strength, and the decreased proton temperature. We also note this small flux rope has been listed as a small transient in Yu et al. (2016). The right figure shows the results of the Lundquist fitting (Huang et al., 2017; Huang et al., 2018; Lundquist, 1950; Wang et al., 2015) of this SFR with the $\chi^2 = 0.81$, suggesting this is a general good small flux rope. Inside the small flux rope, there is a magnetic discontinuity at around 13:10 UT on March 30, where the ϕ_B and the magnetic components all show a large change. We suppose the enhanced anti-sunward streaming ions in region (3) may be attributed to the accelerations of this small flux rope and/or the turbulence and possibly other local small structures. Besides, Gómez-Herrero et al. (2009) have studied the velocity dispersion in CIR events at low energies observed by the SEPT, they indicate the latitudinal separation and temporal evolution may lead to a dispersion in such events. This also support our conclusion that there is local temporal evolution of the SIR event as we can see weak velocity dispersion in region (3). A thorough investigation of local structures on the anisotropies in SIR events is valuable for a future work.

5. Summary

As a conclusion, we report an SIR event in the decay phase of a gradual SEP event, and we further investigate the energy spectra variations associated with the fine structures of this SIR. The main results are summarized below:

1. The SIR is capable of accelerating the ions to around 35 MeV nuc^{-1}, which is nearly two times of the upper limit of the energy as identified by previous observations (e.g., Mason et al., 2008; Richardson, 2004), but they are still of the same order. This is reasonable because the SIR, which appears in the decay phase of the gradual SEP event, could use the energetic ions from the gradual SEP event as seed ions for further accelerations.
2. Two different mechanisms work to accelerate the ions in the SIR event. The intensities of low energy ions peak at the forward-reverse shock pair, whereas the intensities of high energy ions peak at the SI. Combining the detailed study of the energy spectra in different regions, we conclude the low energy ions are accelerated by the shocks, and the high energy ions are accelerated by non-shock associated mechanisms.
3. Significant directional anisotropies are observed in this SIR event, which is uncommon to see in previous SIR events. We find the sunward and anti-sunward streaming ions are much different in different regions and at different energies. According to the analysis, we suggest that the transport effects, the magnetic connection of shocks, and small flux rope may contribute to the anisotropies of the energetic ion intensities.

Our results indicate that the SIR events in the decay phase of gradual SEP events are valuable for further investigations to reveal the origin, acceleration and transport processes of energetic ions. However, it is hard to identify which effect contributes the most based on the current one point observation. A multi-spacecraft study along with numerical simulation from the inner heliosphere to 1 AU is necessary to indicate the evolution of SIR events and figure out the contributions of different processes, this is possible for future work as the Parker Solar Probe, Solar Orbiter, STEREO, and Wind/ACE could form a perfect constellation for conjunct observations that cover different heliocentric distances and longitudes.

Appendix A: Supplementary Figures of the SIR Event

Figure A1 presents a supplementary plot of the SIR event with multi-line format. Panels (B)–(H) in this figure are exactly the same to those in Figure 1. The colored lines in panels (C) to (H) represent the energy channels of the telescopes, whereas the magnitude of each line indicates the ion intensity, except the lines in panel (H) showing the flux anisotropies. The shaded region and vertical lines have the same meanings as those in Figure 1. This figure is a supplement of Figure 1 to reveal the intensity variations of the energetic ions in the SIR event. From this figure, we can also see the main features of this SIR event: (1) The intensity asymmetry is clear around the SI from panels (C) to (G); (2) The intensities of high energy ions are peaked around the SI as shown in panels (C) to (G), whereas the intensities of low energy ions are peaked at the RS as shown in panels (F) and (G); (3) The intensity anisotropies are significant at high energies before the SI, whereas they are more profound at low energies after the SI, as indicated by panel (H).

Figure A2 presents a supplementary plot of the LET observations at different look-directions. Panel (A) to (C) shows the LET proton intensities binned into 16 look-directions (sectors) at high energy channel (HI, 6–10 MeV), low energy channel (LO, 4–6 MeV), and very low energy channel (VLO, 1.8–3.6 MeV), respectively. Panel (D) presents the summed intensities over the sunward and anti-sunward sectors in different energy channels, as indicated by the colored labels. Panel (E) shows the intensity ratios between the sunward and anti-sunward sectors as shown in panel (D). Panel (F) displays the ion intensity anisotropies observed by SEPT, which is the same to panel (H) in Figure 1. From panels (E) and (F), we can clearly see the ion intensity anisotropies shown from the LET observations match well with that from SEPT observations at energies above 0.3 MeV, which is discussed in Section 4.2. Besides, the sectored LET observations only include three energy channels, which is not good enough to fit the energy spectra as compared with the unsectored proton intensities in 12 energy channels. Therefore, we use the unsectored proton intensities from LET to fit the energy spectra, but we add this figure as a supplement for clarification.
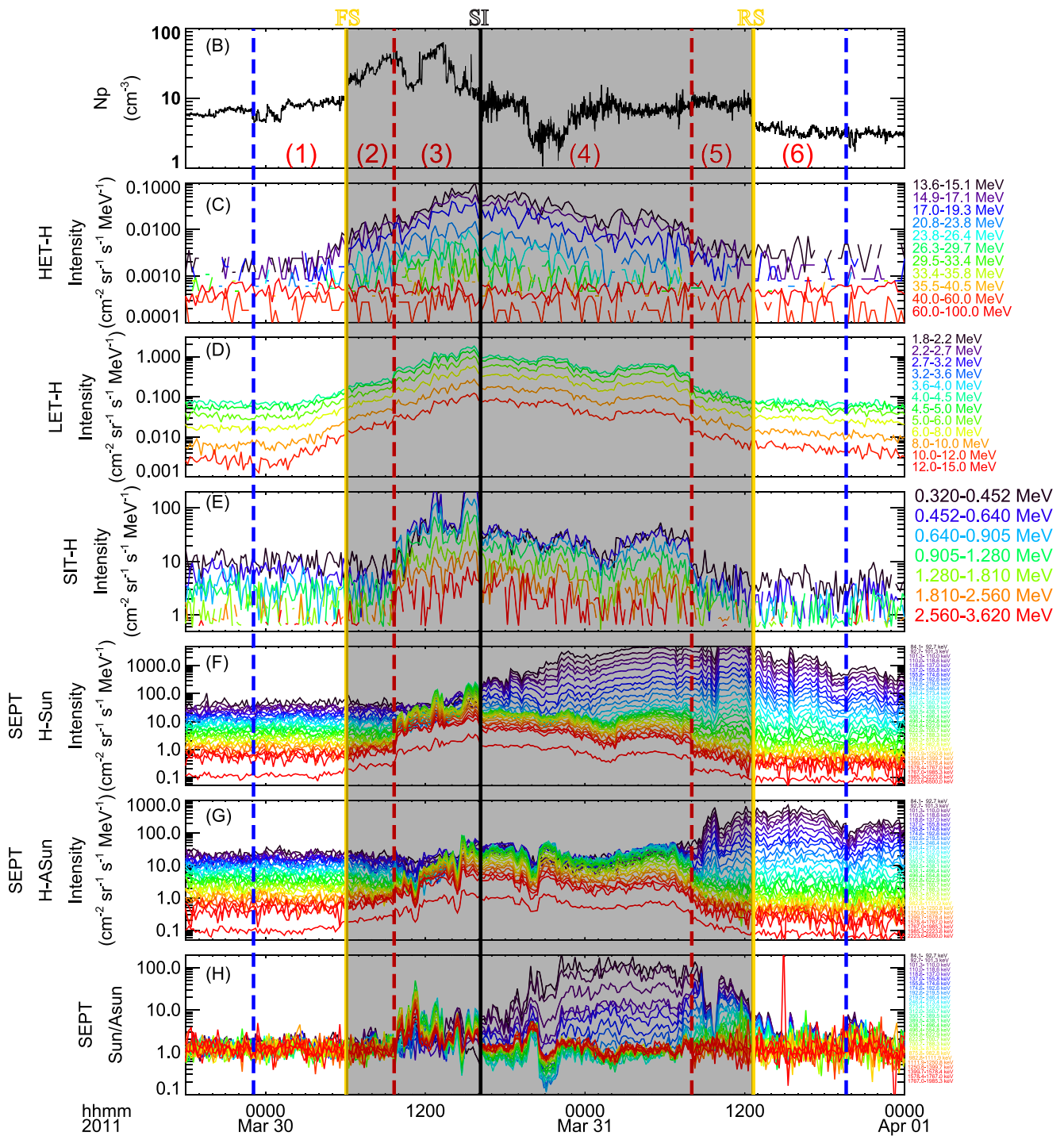
Figure A1. Overview of the SIR event. Panels (b) to (h) show the same parameters as that in Figure 1, but these panels are plotted with a multi-line format except panel (b). The colored lines in panels (c) to (h) represent the energy channels of the telescopes. The shaded region and vertical lines have the same meanings as those shown in Figure 1.
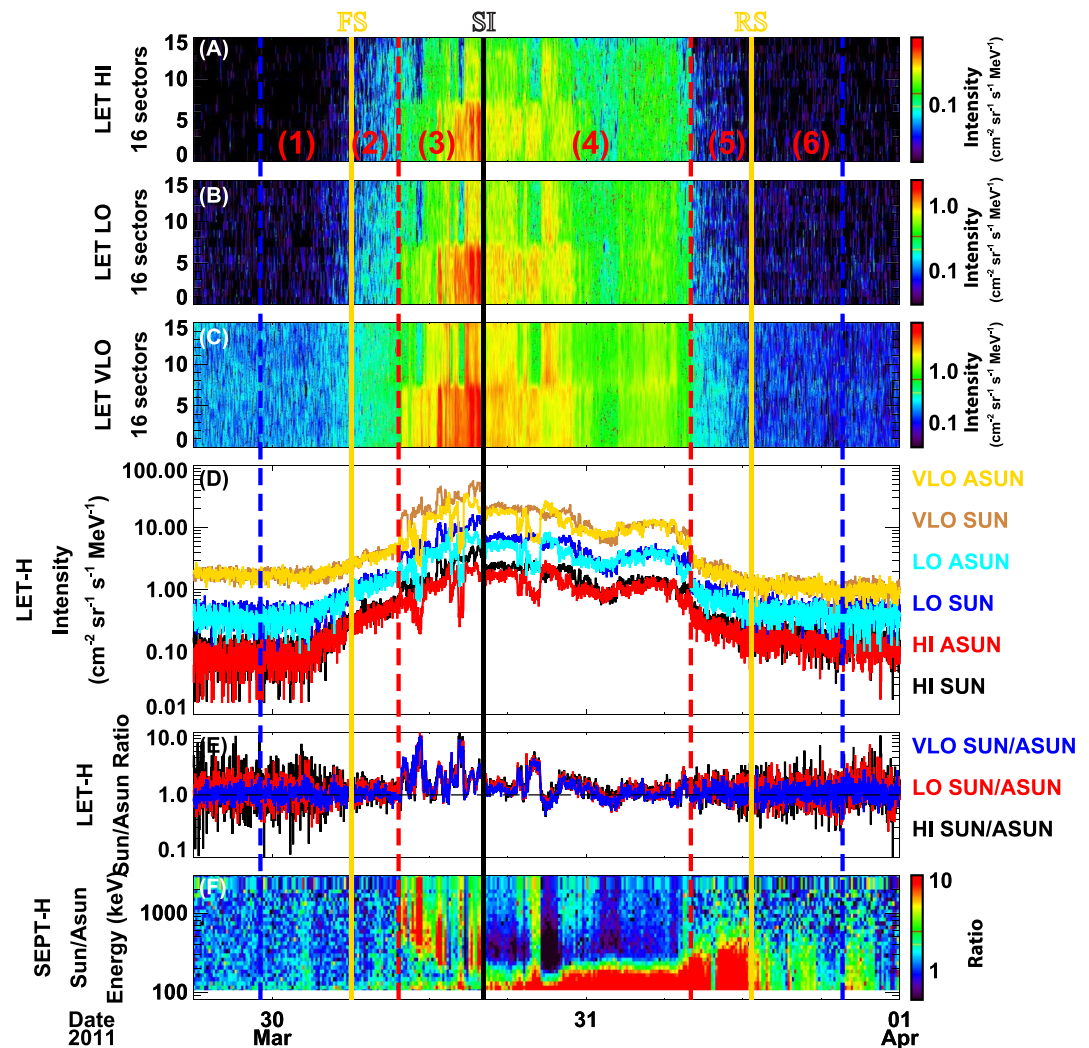
Figure A2. LET observations at different look-directions. Panel (a) to (c) shows the LET proton intensities binned into 16 look-directions (sectors) at high energy channel (HI, 6–10 MeV), low energy channel (LO, 4–6 MeV), and very low energy channel (VLO, 1.8–3.6 MeV), respectively. Panel (d) presents the summed intensities over the sunward and anti-sunward sectors in different energy channels, as indicated by the colored labels. Panel (e) shows the intensity ratios between the sunward and anti-sunward sectors as shown in panel (d). Panel (f) displays the ion intensity anisotropies observed by SEPT, which is the same to panel (h) in Figure 1.

Data Availability Statement

The data for this work are provided by the STEREO Science Center (https://stereo-ssc.nascom.nasa.gov/ins_data.shtml) with details described in the Data section in the paper, and we acknowledge the use of them. The two online catalogs of SIRs and interplanetary shocks observed by STEREO spacecraft are https://stereo-ssc.nascom.nasa.gov/pub/ins_data/impact/level3/SIRs.pdf and https://stereo-ssc.nascom.nasa.gov/pub/ins_data/impact/level3/IPs.pdf, respectively.

References

Acuna, M. H., Curtis, D., Scheifele, J. L., Russell, C. T., Schroeder, P., Szabo, A., & Luhmann, J. G. (2008). *The stereo/impact magnetic field experiment*. Springer.

Balogh, A., Bothmer, V., Crooker, N., Forsyth, R., Gloeckler, G., Hewish, A., et al. (1999). The solar origin of corotating interaction regions and their formation in the inner heliosphere. *Space Science Reviews*, *89*(1), 141–178. https://doi.org/10.1023/A:1005245306874

Belcher, J., & Davis, L., Jr. (1971). Large-amplitude alfvén waves in the interplanetary medium, 2. *Journal of Geophysical Research*, *76*(16), 3534–3563. https://doi.org/10.1029/ja076i016p03534

Chotoo, K., Schwadron, N., Mason, G., Zurbuchen, T., Gloeckler, G., Posner, A., et al. (2000). The suprathermal seed population for corotating interaction region ions at 1 au deduced from composition and spectra of h+, he++, and he+ observed on wind. *Journal of Geophysical Research*, *105*(A10), 23107–23122. https://doi.org/10.1029/1998ja000015

Cohen, C., Christian, E., Cummings, A., Davis, A., Desai, M., Giacalone, J., et al. (2020). Energetic particle increases associated with stream interaction regions. *The Astrophysical Journal - Supplement Series*, *246*(2), 20. https://doi.org/10.3847/1538-4365/ab4c38

Crooker, N., Gosling, J., Bothmer, V., Forsyth, R., Gazis, P., Hewish, A., et al. (1999). Cir morphology, turbulence, discontinuities, and energetic particles. *Space Science Reviews*, *89*(1), 179–220. https://doi.org/10.1023/A:1005253526438

Desai, M., & Giacalone, J. (2016). Large gradual solar energetic particle events. *Living Reviews in Solar Physics*, *13*(3), 1–132. https://doi.org/10.1007/s41116-016-0002-5

Desai, M., Mitchell, D., Szalay, J., Roelof, E., Giacalone, J., Hill, M., et al. (2020). Properties of suprathermal-through-energetic he ions associated with stream interaction regions observed over the parker solar probe's first two orbits. *The Astrophysical Journal - Supplement Series*, *246*(2), 56. https://doi.org/10.3847/1538-4365/ab65ef

Drury, L. O. (1983). An introduction to the theory of diffusive shock acceleration of energetic particles in tenuous plasmas. *Reports on Progress in Physics*, *46*(8), 973–1027. https://doi.org/10.1088/0034-4885/46/8/002

Dwyer, J., Mason, G., Mazur, J., Jokipii, J., Von Rosenvinge, T., & Lepping, R. (1997). Perpendicular transport of low-energy corotating interaction region-associated nuclei. *The Astrophysical Journal Letters*, *490*(1), L115–L118. https://doi.org/10.1086/311003

Ellison, D. C., & Ramaty, R. (1985). Shock acceleration of electrons and ions in solar flares. *The Astrophysical Journal*, *298*, 400–408. https://doi.org/10.1086/163623

Fisk, L. A., & Lee, M. A. (1980). Shock acceleration of energetic particles in corotating interaction regions in the solar wind. *The Astrophysical Journal*, *237*, 620–626. https://doi.org/10.1086/157907

Galvin, A. B., Kistler, L. M., Popecki, M. A., Farrugia, C. J., Simunac, K. D. C., Ellis, L., et al. (2008). The plasma and suprathermal ion composition (PLASTIC) investigation on the STEREO Observatories. *Space Science Reviews*, *136*(1–4), 437–486. https://doi.org/10.1007/s11214-007-9296-x

Giacalone, J., & Jokipii, J. (1997). Spatial variation of accelerated pickup ions at co-rotating interaction regions. *Geophysical Research Letters*, *24*(14), 1723–1726. https://doi.org/10.1029/97gl01631

Giacalone, J., Jokipii, J. R., & Kóta, J. (2002). Particle acceleration in solar wind compression regions. *The Astrophysical Journal*, *573*, 845–850. https://doi.org/10.1086/340660

Gómez-Herrero, R., Klassen, A., Müller-Mellin, R., Heber, B., Wimmer-Schweingruber, R., & Böttcher, S. (2009). Recurrent cir-accelerated ions observed by stereo sept. *Journal of Geophysical Research*, *114*(A5). https://doi.org/10.1029/2008ja013755

Gómez-Herrero, R., Malandraki, O., Dresing, N., Kilpua, E., Heber, B., Klassen, A., et al. (2010). Multi-point observations of cir-associated energetic particles during the 2008 solar minimum. *AIP Conference Proceedings*, *1216*(1), 608–612.

Huang, J., Liu, Y. C.-M., Klecker, B., & Chen, Y. (2016). Coincidence of heliospheric current sheet and stream interface: Implications for the origin and evolution of the solar wind. *Journal of Geophysical Research: Space Physics*, *121*(1), 19–29. https://doi.org/10.1002/2015JA021729

Huang, J., Liu, Y. C.-M., Peng, J., Li, H., Klecker, B., Farrugia, C. J., et al. (2017). A multispacecraft study of a small flux rope entrained by rolling back magnetic field lines. *Journal of Geophysical Research*, *122*, 6927–6939. https://doi.org/10.1002/2017JA023906

Huang, J., Liu, Y. C.-M., Peng, J., Qi, Z., Li, H., Klecker, B., et al. (2018). The distributions of iron average charge states in small flux ropes in interplanetary space: Clues to their twisted structures. *Journal of Geophysical Research: Space Physics*, *123*(9), 7167–7180. https://doi.org/10.1029/2018ja025660

Huang, J., Liu, Y. C.-M., Qi, Z., Klecker, B., Marghitu, O., Galvin, A. B., et al. (2016). A multievent study of the coincidence of heliospheric current sheet and stream interface. *Journal of Geophysical Research: Space Physics*, *121*(11), 768–810. https://doi.org/10.1002/2016JA022842

Intriligator, D., Jokipii, J., Horbury, T., Intriligator, J., Forsyth, R., Kunow, H., et al. (2001). Processes associated with particle transport in corotating interaction regions and near stream interfaces. *Journal of Geophysical Research*, *106*(A6), 10625–10634. https://doi.org/10.1029/2000ja000070

Jian, L., Russell, C., Luhmann, J., Galvin, A., & Simunac, K. (2013). Solar wind observations at stereo: 2007-2011. *AIP Conference Proceedings*, *1539*(1), 191–194. https://doi.org/10.1063/1.4811020

Jian, L., Russell, C., Luhmann, J., & Skoug, R. (2006). Properties of stream interactions at one au during 1995–2004. *Solar Physics*, *239*(1), 337–392. https://doi.org/10.1007/s11207-006-0132-3

Jones, F. C., & Ellison, D. C. (1991). The plasma physics of shock acceleration. *Space Science Reviews*, *58*(1), 259–346. https://doi.org/10.1007/bf01206003

Joyce, C., McComas, D., Christian, E., Schwadron, N., Wiedenbeck, M., McNutt, R., Jr., et al. (2020). Energetic particle observations from the parker solar probe using combined energy spectra from the ISIS instrument suite. *The Astrophysical Journal - Supplement Series*, *246*(2), 41. https://doi.org/10.3847/1538-4365/ab5948

Joyce, C., McComas, D., Schwadron, N., Christian, E., Wiedenbeck, M., McNutt, R., et al. (2021). Time evolution of stream interaction region energetic particle spectra in the inner heliosphere. *Astronomy & Astrophysics*, *650*, L5. https://doi.org/10.1051/0004-6361/202039330

Kaiser, M. L., Kucera, T., Davila, J., Cyr, O. S., Guhathakurta, M., & Christian, E. (2008). The stereo mission: An introduction. *Space Science Reviews*, *136*(1), 5–16. https://doi.org/10.1007/s11214-007-9277-0

Kocharov, L., Kovaltsov, G. A., Torsti, J., Anttila, A., & Sahla, T. (2003). Modeling the propagation of solar energetic particles in corotating compression regions of solar wind. *JGR*, *108*, 1404. https://doi.org/10.1029/2003JA009928

Kocharov, L., Pizzo, V. J., Odstrcil, D., & Zwickl, R. D. (2009). A unified model of solar energetic particle transport in structured solar wind. *JGR*, *114*, A05102. https://doi.org/10.1029/2008JA013837

Lee, M. A., Mewaldt, R., & Giacalone, J. (2012). Shock acceleration of ions in the heliosphere. *Space Science Reviews*, *173*(1), 247–281. https://doi.org/10.1007/s11214-012-9932-y

Le Roux, J., Zank, G., Webb, G., & Khabarova, O. (2015). A kinetic transport theory for particle acceleration and transport in regions of multiple contracting and reconnecting inertial-scale flux ropes. *The Astrophysical Journal*, *801*(2), 112. https://doi.org/10.1088/0004-637x/801/2/112

Li, G. (2017). Particle acceleration and transport in the inner heliosphere. *Science China Earth Sciences*, *60*, 1440–1465. https://doi.org/10.1007/s11430-017-9083-y

Liu, Z., Wang, L., Wimmer-Schweingruber, R. F., Krucker, S., & Mason, G. M. (2020). Pan-spectrum fitting formula for suprathermal particles. *Journal of Geophysical Research*, *125*(12). https://doi.org/10.1029/2020JA028702

Luhmann, J. G., Curtis, D. W., Schroeder, P., McCauley, J., Lin, R. P., Larson, D. E., et al. (2008). STEREO IMPACT investigation goals, measurements, and data Products overview. *Space Science Reviews*, *136*(1–4), 117–184. https://doi.org/10.1007/s11214-007-9170-x

Lundquist, S. (1950). Magnetohydrostatic fields. *Ark. Fys.*, *2*, 361–365.

Malandraki, O. E., & Crosby, N. B. (2018). Solar energetic particles and space weather: Science and applications. In *Solar particle radiation storms forecasting and analysis* (pp. 1–26). Springer. https://doi.org/10.1007/978-3-319-60051-2_1

Markwardt, C. (2009). Non-linear least-squares fitting in idl with mpfit. *Astronomical data analysis software and systems xviii*, *411*, 251.

Mason, G., Von Steiger, R., Decker, R., Desai, M., Dwyer, J., Fisk, L., et al. (1999). Origin, injection, and acceleration of CIR particles: Observations. Corotating Interaction Regions, 327–367. https://doi.org/10.1007/978-94-017-1179-1_16

Mason, G. M., Korth, A., Walpole, P. H., Desai, M. I., Von Rosenvinge, T. T., & Shuman, S. A. (2008). The suprathermal ion telescope (SIT) for the IMPACT/SEP investigation. *Space Science Reviews*, *136*(1–4), 257–284. https://doi.org/10.1007/s11214-006-9087-9

Mason, G. M., Leske, R. A., Desai, M. I., Cohen, C., Dwyer, J. R., Mazur, J. E., et al. (2008). Abundances and energy spectra of corotating interaction region heavy ions observed during solar cycle 23. *The Astrophysical Journal*, *678*(2), 1458–1470. https://doi.org/10.1086/533524

Mason, G. M., Li, G., Cohen, C. M. S., Desai, M. I., Haggerty, D. K., Leske, R. A., et al. (2012). Interplanetary propagation of solar energetic particle heavy ions observed at 1 AU and the role of energy scaling. *The Astrophysical Journal*, *761*, 104. https://doi.org/10.1088/0004-637X/761/2/104

McComas, D., Christian, E., Cohen, C., Cummings, A., Davis, A., Desai, M., et al. (2019). Probing the energetic particle environment near the sun. *Nature*, *576*(7786), 223–227. https://doi.org/10.1038/s41586-019-1811-1

Mewaldt, R., Cohen, C., Mason, G., Von Rosenvinge, T., Leske, R., Luhmann, J., et al. (2013). Solar energetic particles and their variability from the sun and beyond. *Solar Wind*, *13*(1539), 116–121. https://doi.org/10.1063/1.4811002

Mewaldt, R., Looper, M., Cohen, C., Haggerty, D., Labrador, A., Leske, R., et al. (2012). Energy spectra, composition, and other properties of ground-level events during solar cycle 23. *Space Science Reviews*, *171*(1–4), 97–120. https://doi.org/10.1007/s11214-012-9884-2

Mewaldt, R. A., Cohen, C. M. S., Cook, W. R., Cummings, A. C., Davis, A. J., Geier, S., et al. (2008). The low-energy telescope (LET) and SEP Central Electronics for the STEREO mission. *Space Science Reviews*, *136*(1–4), 285–362. https://doi.org/10.1007/s11214-007-9288-x

Müller-Mellin, R., Böttcher, S., Falenski, J., Rode, E., Duvet, L., Sanderson, T., et al. (2008). The solar electron and proton telescope for the stereo mission. *The STEREO Mission*, *136*, 363–389. https://doi.org/10.1007/s11214-007-9204-4

Ng, C. (2014). Effect of solar-wind velocity, magnetic field and density on solar energetic particle transport. *Outstanding Problems in Heliophysics: From Coronal Heating to the Edge of the Heliosphere*, *484*, 156.

Park, J., Innes, D., Bucik, R., & Moon, Y.-J. (2013). The source regions of solar energetic particles detected by widely separated spacecraft. *The Astrophysical Journal*, *779*(2), 184. https://doi.org/10.1088/0004-637X/779/2/184

Qin, G., Zhang, M., & Dwyer, J. R. (2006). Effect of adiabatic cooling on the fitted parallel mean free path of solar energetic particles. *JGR*, *111*, A08101. https://doi.org/10.1029/2005JA011512

Reames, D. V. (1999). Particle acceleration at the Sun and in the heliosphere. *Space Science Reviews*, *90*, 413–491. https://doi.org/10.1023/A:1005105831781

Richardson, I., Rosenvinge, T., Cane, H., Christian, E., Cohen, C., Labrador, A., et al. (2014). 25 mev proton events observed by the high energy telescopes on the stereo a and b spacecraft and/or at Earth during the first seven years of the stereo mission. *Solar Physics*, *8*(289), 3059–3107. https://doi.org/10.1007/s11207-014-0524-8

Richardson, I. G. (2004). Energetic particles and corotating interaction regions in the solar wind. *Space Science Reviews*, *111*, 267–376. https://doi.org/10.1023/b:spac.0000032689.52830.3e

Richardson, I. G. (2018). Solar wind stream interaction regions throughout the heliosphere. *Living Reviews in Solar Physics*, *15*(1), 1. https://doi.org/10.1007/s41116-017-0011-z

Rouillard, A. P., Sheeley, N. R., Tylka, A., Vourlidas, A., Ng, C. K., Rakowski, C., et al. (2012). The longitudinal properties of a solar energetic particle event investigated using modern solar imaging. *The Astrophysical Journal*, *752*(1), 44. https://doi.org/10.1088/0004-637x/752/1/44

Ruffolo, D. (1995). Effect of adiabatic deceleration on the focused transport of solar cosmic rays. *The Astrophysical Journal*, *442*, 861–874. https://doi.org/10.1086/175489

Sauvaud, J.-A., Larson, D., Aoustin, C., Curtis, D., Médale, J.-L., Fedorov, A., et al. (2008). The impact solar wind electron analyzer (swea). *The STEREO Mission*, *136*, 227–239. https://doi.org/10.1007/s11214-007-9174-6

Schure, K., Bell, A., O'C Drury, L., & Bykov, A. (2012). Diffusive shock acceleration and magnetic field amplification. *Space Science Reviews*, *173*(1), 491–519. https://doi.org/10.1007/s11214-012-9871-7

Schwadron, N., Fisk, L., & Gloeckler, G. (1996). Statistical acceleration of interstellar pick-up ions in co-rotating interaction regions. *Geophysical Research Letters*, *23*(21), 2871–2874. https://doi.org/10.1029/96gl02833

Schwadron, N., Joyce, C., Aly, A., Cohen, C., Desai, M., McComas, D., et al. (2021). A new view of energetic particles from stream interaction regions observed by parker solar probe. *Astronomy & Astrophysics*, *650*, A24. https://doi.org/10.1051/0004-6361/202039352

Sokolov, I., Roussev, I., Fisk, L., Lee, M., Gombosi, T., & Sakai, J. (2006). Diffusive shock acceleration theory revisited. *The Astrophysical Journal Letters*, *642*(1), L81–L84. https://doi.org/10.1086/504406

Tylka, A., Cohen, C., Dietrich, W., Lee, M., Maclennan, C., Mewaldt, R., et al. (2005). Shock geometry, seed populations, and the origin of variable elemental composition at high energies in large gradual solar particle events. *The Astrophysical Journal*, *625*(1), 474–495. https://doi.org/10.1086/429384

Von Rosenvinge, T. T., Reames, D. V., Baker, R., Hawk, J., Nolan, J. T., Ryan, L., et al. (2008). The high energy telescope for STEREO. *Space Science Reviews*, *136*(1–4), 391–435. https://doi.org/10.1007/s11214-007-9300-5

Wang, Y., Qin, G., & Zhang, M. (2012). Effects of perpendicular diffusion on energetic particles accelerated by the interplanetary coronal mass ejection shock. *The Astrophysical Journal*, *752*, 37. https://doi.org/10.1088/0004-637X/752/1/37

Wang, Y., Zhou, Z., Shen, C., Liu, R., & Wang, S. (2015). Investigating plasma motion of magnetic clouds at 1 au through a velocity-modified cylindrical force-free flux rope model. *Journal of Geophysical Research: Space Physics*, *120*(3), 1543–1565. https://doi.org/10.1002/2014JA020494

Wei, W., Shen, F., Yang, Z., Zhao, L., Wang, Y., Zuo, P., & Zhang, J. (2019). Modeling solar energetic particle transport in 3d background solar wind: Influences of the compression regions. *Journal of Atmospheric and Solar-Terrestrial Physics*, *182*, 155–164. https://doi.org/10.1016/j.jastp.2018.11.012

Wu, Z., Chen, Y., Li, G., Zhao, L. L., Ebert, R. W., Desai, M. I., et al. (2014). Observations of energetic particles between a pair of corotating interaction regions. *The Astrophysical Journal*, *781*, 17. https://doi.org/10.1088/0004-637X/781/1/17

Yang, L., Wang, L., Li, G., Wimmer-Schweingruber, R. F., He, J., Tu, C., et al. (2019). Electron acceleration by icme-driven shocks at 1 au. *The Astrophysical Journal*, *875*(2), 104. https://doi.org/10.3847/1538-4357/ab1133

Yu, W., Farrugia, C. J., Galvin, A., Lugaz, N., Luhmann, J., Simunac, K., & Kilpua, E. (2016). Small solar wind transients at 1 au: Stereo observations (2007–2014) and comparison with near-Earth wind results (1995–2014). *Journal of Geophysical Research: Space Physics*, *121*(6), 5005–5024. https://doi.org/10.1002/2016JA022642

Zank, G., Hunana, P., Mostafavi, P., Le Roux, J., Li, G., Webb, G., et al. (2015). Diffusive shock acceleration and reconnection acceleration processes. *The Astrophysical Journal*, *814*(2), 137. https://doi.org/10.1088/0004-637x/814/2/137

Zhang, M., Qin, G., & Rassoul, H. (2009). Propagation of solar energetic particles in three-dimensional interplanetary magnetic fields. *The Astrophysical Journal*, *692*, 109–132. https://doi.org/10.1088/0004-637X/692/1/109

Zhao, L., Li, G., Ebert, R. W., Dayeh, M. A., Desai, M. I., Mason, G. M., et al. (2016). Modeling transport of energetic particles in corotating interaction regions: A case study. *JGR*, *121*, 77–92. https://doi.org/10.1002/2015JA021762

Zhao, L.-L., Zank, G., Chen, Y., Hu, Q., Le Roux, J., Du, S., & Adhikari, L. (2019). Particle acceleration at 5 au associated with turbulence and small-scale magnetic flux ropes. *The Astrophysical Journal*, *872*(1), 4. https://doi.org/10.3847/1538-4357/aafcb2

Zharkova, V. V., & Khabarova, O. V. (2012). Particle dynamics in the reconnecting heliospheric current sheet: Solar wind data versus three-dimensional particle-in-cell simulations. *The Astrophysical Journal*, *752*(1), 35. https://doi.org/10.1088/0004-637x/752/1/35